

<https://doi.org/10.1038/s41514-025-00197-1>

# Calcium ( $\text{Ca}^{2+}$ ) fluxes at mitochondria-ER contact sites (MERCS) are a new target of senolysis in therapy-induced senescence (TIS)

Check for updates

Andrea Puebla-Huerta<sup>1,2,17</sup>, Hernán Huerta<sup>1,2,17</sup>, Camila Quezada-Gutiérrez<sup>1,2</sup>, Pablo Morgado-Cáceres<sup>1,2</sup>, César Casanova-Canelo<sup>1,2</sup>, Sandra A. Niño<sup>1,2,3</sup>, Sergio Linsambarth<sup>1,2</sup>, Osman Díaz-Rivera<sup>1,2</sup>, José Alberto López-Domínguez<sup>4</sup>, Sandra Rodríguez-López<sup>1,2</sup>, José Antonio González-Reyes<sup>1,2</sup>, Galdo Bustos<sup>1,2</sup>, Eduardo Silva-Pavez<sup>1,16</sup>, Alenka Lovy<sup>1,2,6</sup>, Gabriel Quiroz<sup>2</sup>, Catalina González-Seguel<sup>1</sup>, Edison Salas-Huenuleo<sup>7</sup>, Marcelo J. Kogan<sup>8,9</sup>, Jordi Molgó<sup>10</sup>, Armen Zakarian<sup>11</sup>, José M. Villalba<sup>1,2</sup>, Christian Gonzalez-Billault<sup>1,2,3,12,13,14</sup>, Tito Cali<sup>15</sup>, Ulises Ahumada-Castro<sup>1,2,16,18</sup> & J. César Cárdenas<sup>1,2,11,18</sup>

Therapy-induced senescence (TIS) alters calcium ( $\text{Ca}^{2+}$ ) flux and Mitochondria-ER Contact Sites (MERCS), revealing critical vulnerabilities in senescent cells. In this study, TIS was induced using Doxorubicin and Etoposide, resulting in an increased MERCS contact surface but a significant reduction in ER-mitochondria  $\text{Ca}^{2+}$  flux. Mechanistically, TIS cells exhibit decreased expression of IP3R isoforms and reduced interaction between type 1 IP3R and VDAC1, impairing  $\text{Ca}^{2+}$  transfer. This flux is crucial for maintaining the viability of senescent cells, highlighting its potential as a therapeutic target. Inhibition of ER-mitochondria  $\text{Ca}^{2+}$  flux demonstrates senolytic effects both in vitro and in vivo, offering a novel strategy for targeting senescent cells.

Cellular senescence, in its canonical manifestation, is characterized by the cessation of the replicative capacity and the development of a distinctive altered phenotype. This phenotype encompasses modifications in the secretome, activation of tumor suppressor genes, alterations in chromatin and genome integrity<sup>1</sup>, induction of senescence-associated  $\beta$ -galactosidase

activity, and metabolic alterations, particularly associated to mitochondria<sup>2</sup>. Specifically, these alterations encompass a mitochondrial network imbalance, changes in mitochondrial membrane potential and electron transport chain, and dysregulation<sup>3</sup>. It is interesting to mention that various types of cellular senescence have been identified, including replicative senescence,

<sup>1</sup>Center for Integrative Biology, Faculty of Sciences, Universidad Mayor, Santiago, Chile. <sup>2</sup>Geroscience Center for Brain Health and Metabolism, Santiago, Chile.

<sup>3</sup>Department of Biology, Laboratory of Cellular and Neuronal Dynamics, Faculty of Sciences, Universidad de Chile, Santiago, Región Metropolitana, Chile. <sup>4</sup>Instituto de Biología Molecular y Celular del Cáncer and Centro de Investigación del Cáncer de Salamanca, University of Salamanca-CSIC, Salamanca, Spain. <sup>5</sup>Departamento de Biología Celular, Fisiología e Inmunología, Universidad de Córdoba, Campus de Excelencia Internacional Agroalimentario, CeIa3, Córdoba, Spain. <sup>6</sup>Department of Ophthalmology and Visual Sciences Center for Vision Research, SUNY Upstate Medical University, Syracuse, USA. <sup>7</sup>Advanced Integrated Technologies (AINTECH), Santiago, Chile. <sup>8</sup>Departamento de Química Farmacológica y Toxicológica, Facultad de Ciencias Químicas y Farmacéuticas, Universidad de Chile, Santos Dumont, Santiago, Chile. <sup>9</sup>Advanced Center of Chronic Diseases (ACCDiS), Santiago, Chile. <sup>10</sup>Université Paris-Saclay, CEA, Département Médicaments et Technologies pour la Santé, Service d'Ingénierie Moléculaire pour la Santé (SIMoS), Equipe Mixte de Recherche CNRS 9004, Gif-sur-Yvette, France. <sup>11</sup>Department of Chemistry and Biochemistry, University of California Santa Barbara, Santa Barbara, CA, USA. <sup>12</sup>Department of Neuroscience, Faculty of Medicine, Universidad de Chile, Santiago, Chile. <sup>13</sup>Public Health Unit, Institute for Nutrition and Food Technology (INTA), Universidad de Chile, Santiago, Chile. <sup>14</sup>The Buck Institute for Research on Aging, Novato, CA, USA. <sup>15</sup>Department of Biomedical Sciences, University of Padua, Padua, Italy; Centro Studi per la Neurodegenerazione (CESNE), University of Padua, Padua, Italy; Neuroscience Center (PNC), University of Padua, Padua, Italy. <sup>16</sup>Present address: Facultad de Odontología y Ciencias de la Rehabilitación, Universidad San Sebastián, Bellavista, Santiago, Chile. <sup>17</sup>These authors contributed equally: Andrea Puebla-Huerta, Hernán Huerta. <sup>18</sup>These authors jointly supervised this work: Ulises Ahumada-Castro, J. César Cárdenas. e-mail: [ulises.ahumada@uss.cl](mailto:ulises.ahumada@uss.cl); [julio.cardenas@umayor.cl](mailto:julio.cardenas@umayor.cl)

oncogene-induced senescence (OIS), and therapy-induced senescence (TIS).

A pivotal event that dictates mitochondrial function is the influx of calcium ( $\text{Ca}^{2+}$ ) ions into the mitochondria.  $\text{Ca}^{2+}$  primarily permeates the mitochondria from the endoplasmic reticulum (ER) through micro-domains where there exists a proximity between mitochondria and the ER, forming quasi-synaptic junctions known as mitochondria-ER contact sites (MERCS). These MERCS typically exhibit a thickness ranging from 10 to 50 nm.  $\text{Ca}^{2+}$  released from the ER is mediated by the inositol 1,4,5-trisphosphate (InsP3) receptors (InsP3Rs) and Ryanodine Receptors (RyR), allowing  $\text{Ca}^{2+}$  to enter the mitochondria. Initially,  $\text{Ca}^{2+}$  passes through the Voltage Dependent Anion Channel (VDAC) located in the outer mitochondrial membrane before reaching the mitochondrial  $\text{Ca}^{2+}$  uniporter complex (MCUC) situated in the inner mitochondrial membrane.<sup>4</sup>

Enhanced MERCS, and increased ER-mitochondria  $\text{Ca}^{2+}$  fluxes have been documented in specific types of senescent cells<sup>5-8</sup>. However, the specificities regarding chemotherapy-induced senescence, herein denoted as TIS cells, remain obscure. To gain further insight on  $\text{Ca}^{2+}$  flux in senescent cells, we initially established a TIS model. We used growing human diploid IMR-90 fibroblasts which were treated with two chemotherapeutic drugs, Doxorubicin [Doxo] (250 nM) and Etoposide [Eto] (40  $\mu\text{M}$ ) over 48 h. Ten days after both treatments the cells were harvested for experiments (Fig. 1A). The evaluation in both groups of cells with well-established senescence markers showed an arrest of cell proliferation with an increase in the expression of negative regulators of the cell cycle p16 and p21 (Fig. 1B). Also, increased SA- $\beta$ -gal positive cells (Fig. 1C) and an increase of several components of the SASP that include IL6, IL1 $\alpha$ , IL1 $\beta$ , CXCL1 and MMP3 (Fig. 1D) was also observed. In this firmly established TIS cell model, we investigated the proximity between ER and mitochondrial membranes using confocal microscopy as an initial approach, noting an increase in ER-mitochondria proximity in both Doxo and Eto-induced TIS (Colocalization Index Manders: Control:  $0.5 \pm 0.03$ ; Doxorubicin:  $0.7 \pm 0.03$ ; Etoposide:  $0.7 \pm 0.01$ ) (Fig. 1E). Note that TIS triggered by Doxo and Eto is characterized by hyperfused mitochondria, consistent with previous observations in senescent cells (<https://doi.org/10.1111/febs.16361>). Considering the confocal microscopy's limited resolution of 250 nm, and the fact that the ER-mitochondria distance associated with MERCS falls within a range of 10 to 50 nm, we opted for transmission electron microscopy (TEM) analysis, acknowledged as the gold standard technique, to assess the percentage of MERCS coverage and the distance between ER and mitochondria (Fig. 1F). Similarly, as shown with confocal microscopy, both Doxo and Eto-induced TIS shows an increase percentage of MERCS coverage, with respect to growing cells (CT:  $19.3 \pm 1.9\%$ ; Doxo:  $35.3 \pm 2.7\%$ ; Eto:  $45.6 \pm 2.3\%$ ). Interestingly, the distance between ER and mitochondria shows a small but consistent increase in both Doxo and Eto-induced TIS with respect to growing cells (CT:  $3.0, 13 \pm 0.9$  nm; Doxo:  $33, 25 \pm 1.0$  nm; Eto:  $33, 25 \pm 0.8$  nm).

To assess the  $\text{Ca}^{2+}$  flux between the ER and mitochondria, we evaluated mitochondrial  $\text{Ca}^{2+}$  uptake using two approaches: Rhod-2AM and the protein sensor MitoGCaMP5. Surprisingly, both TIS cell models exhibited decreased mitochondrial  $\text{Ca}^{2+}$  uptake following stimulation with histamine, an inducer of  $\text{Ca}^{2+}$  release mediated by IP3R (Fig. 1G). The dissipation of the mitochondrial membrane potential using FCCP in cells loaded with Fluo-4AM demonstrates that Doxo-induced TIS cells exhibit a higher mitochondrial  $\text{Ca}^{2+}$  concentration (Fig. 1H). This observation was further confirmed using the mitochondria-targeted ratio-metric  $\text{Ca}^{2+}$  sensor GEM-GECO1<sub>mito</sub>, where ratio measurements ( $F_{(470-500)}/F_{(>515)}$ ) revealed a significant elevation in resting mitochondrial  $\text{Ca}^{2+}$  concentration in Doxo-induced TIS cells compared to controls (Fig. 1I). Measurement of cytosolic  $\text{Ca}^{2+}$  using Fluo-4AM revealed a concurrent decrease in IP3R-mediated  $\text{Ca}^{2+}$  release from the ER in both TIS cell models (Fig. 1J). All our  $\text{Ca}^{2+}$  measurements were performed in  $\text{Ca}^{2+}$ -free media.

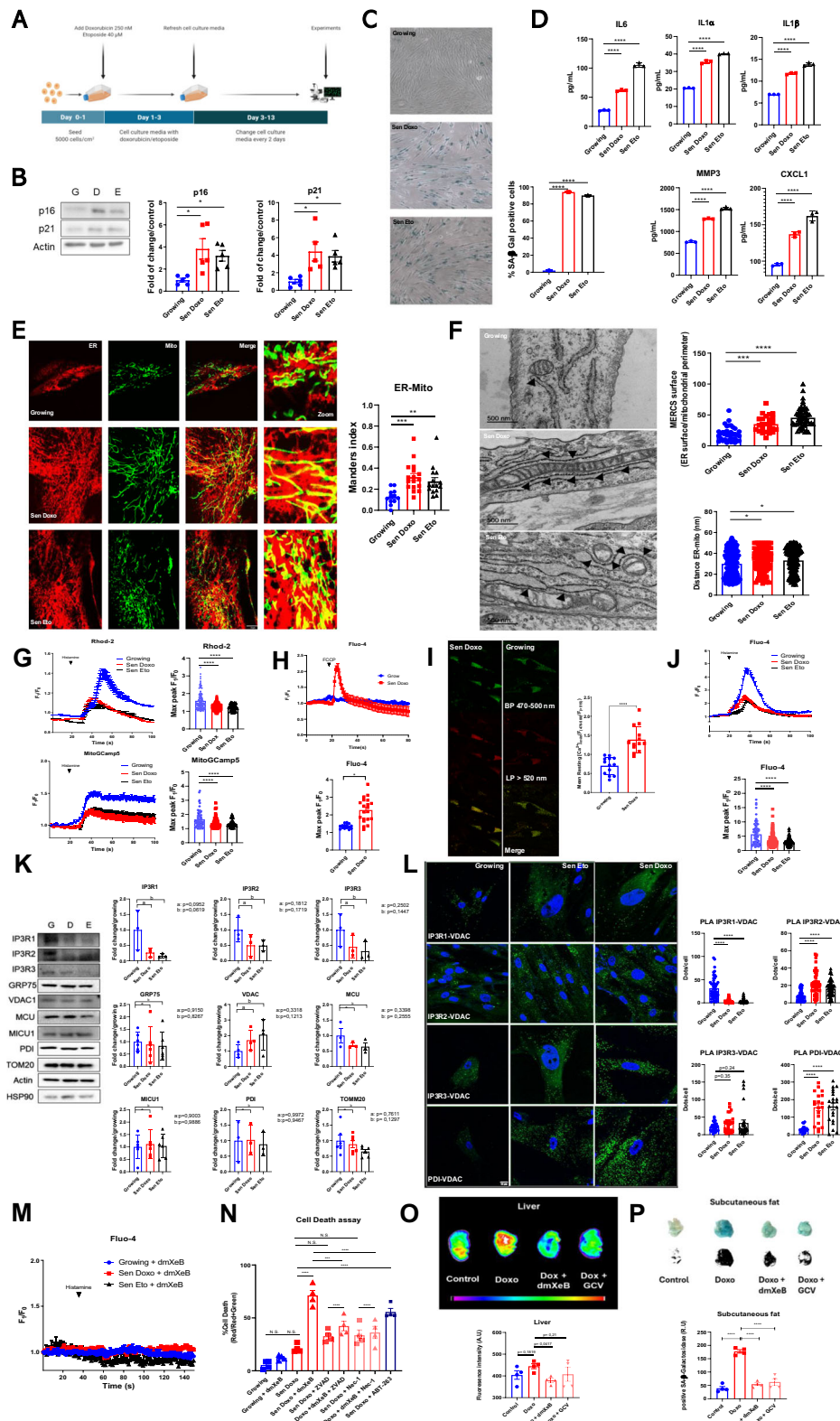
To unravel the underlying mechanisms responsible for the reduced ER  $\text{Ca}^{2+}$  release and transfer to the mitochondria, we scrutinized the levels of

well-characterized MERCS resident proteins, particularly those implicated with ER-mitochondria  $\text{Ca}^{2+}$  flux. Intriguingly, we observed a strong level decrease trend of the three IP3R isoforms in both TIS cell models compared to growing cells, while other resident proteins such as GRP75, VDAC, MCU, MICU1, PDI, and TOMM20 did not show statistically significant changes (Fig. 1K). Furthermore, employing Proximity Ligation Assay (PLA), we detected reduced proximity between IP3R and VDAC (PLA IP3R1-VDAC) in both TIS cell models compared to control growing cells. Intriguingly, the PLA assay revealed an increase in proximity between IP3R2 and VDAC (PLA IP3R2-VDAC) and the ER resident protein PDI and VDAC (PLA PDI-VDAC) (Fig. 1L). Altogether, our findings indicate that both TIS cell models are characterized by an increase in structural interactions between ER and mitochondria. Notably, these interactions specifically exclude type 1 IP3R isoform, resulting in a reduced  $\text{Ca}^{2+}$  flux between the ER and mitochondria.

Our group has previously demonstrated the critical role of the  $\text{Ca}^{2+}$  flux between the ER and mitochondria is crucial in cell survival. Given our observation of a decrease in  $\text{Ca}^{2+}$  flux between the ER and mitochondria, we aimed to assess the essentiality of this  $\text{Ca}^{2+}$  flux becomes for TIS cells. To this end, we used desmethyl XeB (dmXeB), a competitive and selective inhibitor of IP3R, which has been reported to affect the viability of tumor cells<sup>9</sup>. After confirming that dmXeB inhibits  $\text{Ca}^{2+}$  release from the ER in both growing and TIS cells (Fig. 1M), we proceeded to evaluate its effect on cell viability. As seen in Fig. 1N, dmXeB does not affect the viability of growing cells, but it does affect the viability of Doxo and Eto-induced TIS cells similarly as ABT-263, a well-known senolytic<sup>10</sup>. Interestingly, cell death caused by dmXeB can be partially reversed using the necroptosis inhibitor Nec-1 and the caspase pan-inhibitor ZVAD. (Fig. 1N). Finally, to investigate whether dmXeB may exert a senolytic effect in vivo, we utilized 20-month-old p16-3MR transgenic mice, which allow for the visualization and elimination of senescent cells upon treatment with Ganciclovir<sup>11</sup>. TIS was induced by 2 rounds of Doxo followed by either 4 rounds of dmXeB or Ganciclovir. Fluorescence intensity associated with the senescence marker p16 significantly decreased in the livers of mice treated with dmXeB (Fig. 1O). Additionally, in the same mice, we evaluated SA- $\beta$ -Galactosidase staining in subcutaneous fat. Similar to the liver, there is a significant decrease in the mice treated with dmXeB, as well as in those treated with GCV (Fig. 1P). Taken together, these results suggest that reducing  $\text{Ca}^{2+}$  flux between the ER and mitochondria is a target for senolysis in the contexts of TIS, and dmXeB emerges as a promising senolytic agent.

MERCS have been recognized as crucial communication platforms orchestrating various cellular processes, including metabolism and apoptosis<sup>4</sup>. In the context of oncogene-induced (OIS), oxidative stress-induced senescence (OSIS) and replicative senescence (RS), some groups demonstrated an increase in MERCS interaction surfaces, concomitant with elevated  $\text{Ca}^{2+}$  flux between the ER and mitochondria, that served as triggering factor for senescence<sup>5-8</sup>. However, the involvement of MERCS in TIS remains unexplored to date. We hypothesize that these differences are associated with the basal levels of mitochondrial  $\text{Ca}^{2+}$  and the duration of exposure to elevated  $\text{Ca}^{2+}$  levels. Prolonged exposure to high mitochondrial  $\text{Ca}^{2+}$  may activate a compensatory mechanism that reduces mitochondrial  $\text{Ca}^{2+}$  uptake, potentially as a protective response to prevent mitochondrial dysfunction or cell death.

Here, we unveil that in TIS, MERCS increase as observed in previous studies; nevertheless, the flux of  $\text{Ca}^{2+}$  between the ER and mitochondria is diminished. This discrepancy may stem from differences in the nature of the senescence inducers, the time frame post-treatment (12 days in our case), and/or the 3% oxygen concentration utilized for cell culture in this study. These oxygen concentrations have been described as normoxic in tissues<sup>12</sup>, in addition to showing a decrease in the impact of replicative senescence associated with 21% oxygen<sup>13,14</sup>. The observed reduction in  $\text{Ca}^{2+}$  flux during TIS aligns with an additional anti-apoptotic mechanism. Madreiter-Sokolowski et al. highlighted that alterations in  $\text{Ca}^{2+}$  flux between the ER and mitochondria are tightly associated with anti-apoptotic processes, as



such changes can render senescent cells more susceptible to apoptosis<sup>7</sup>. Notably, their study demonstrated that resveratrol significantly increased mitochondrial  $\text{Ca}^{2+}$  uptake in senescent cells, leading to reduced cell viability and activation of apoptotic caspase 3/7 activity. Similarly, in our models, the use of dmXeB, which inhibits  $\text{Ca}^{2+}$  flux between the ER and mitochondria, induces apoptotic-like phenomena.

An interesting observation is the switch in interaction between VDAC and IP3R1 and 2, with IP3R1 decreasing and IP3R2 increasing. IP3Rs function as heterotetramers with stoichiometries that may vary depending on cell type and context, influencing their sensitivities to IP3. Another noteworthy aspect of the different isoforms is their varied roles in receptor licensing. It remains to be elucidated whether, in the context of senescence,

**Fig. 1 | Therapy induces senescence (TIS) increase MERCS, but decreases the ER-mitochondria  $\text{Ca}^{2+}$  flux, which becomes essential for TIS cell survival.**

**A** Schematic diagram of induction and establishment of therapy-induced senescence. **B** Representative Western blot of p16 and p21 in growing and senescence cells induce with doxorubicin (Sen Doxo) and etoposide (Sen Eto). Bar graph: p16/actin and p21/actin expressed as average fold change over basal levels (growing cells).  $N = 5$ , Mean  $\pm$  S.E.,  $*p < 0.05$  (ANOVA Test). **C** Representative images of SA- $\beta$ -gal staining in growing, Sen Doxo and Sen Eto and quantitative analysis of stained cells (100 cells per N,  $N = 3$ ;  $****p \leq 0.0001$ , ANOVA test). Bar: 50  $\mu\text{m}$ . **D** Concentration of IL6, IL-1 $\alpha$ , IL-1 $\beta$ , MMP3, CXCL1, determined by Luminex assay in supernatant of growing, Sen Doxo and Sen Eto cells. ( $N = 3$ ,  $****p \leq 0.0001$ , ANOVA Test). **E** Representative images of growing, Sen Doxo and Sen Eto labeled with KDEL-BFP to visualize ER and 100 nM TMRE to visualize mitochondria. Bar: 10  $\mu\text{m}$ . Bar graph: Manders index as an indicator of colocalization (20 – 30 cells per N;  $N = 3$ ;  $**p \leq 0.01$   $***p \leq 0.005$ , ANOVA test). **F** Representative TEM images and quantification of contact surface area between ER and mitochondria and the distance between ER and mitochondria in growing sen Doxo and Sen Eto. Arrow heads show MERCS ( $N = 3$ , 50–70 mitochondria per N,  $*p < 0.05$ , ANOVA test). **G** Representative traces of mitochondrial  $\text{Ca}^{2+}$  responds in growing, Sen Doxo and Sen Eto cells challenge with histamine using Rhod-2AM and MitoGCamp5. Bar graphs: Quantification of peak Rhod-2AM ( $N = 3$ , Mean  $\pm$  SEM. 50–80 cells were analyzed in each experiment) and MitoGCamp5 ( $N = 3$ , mean  $\pm$  SEM. 20 cells were analyzed in each experiment) fluorescence.  $****p \leq 0.0001$ , ANOVA test). **H** Representative traces of cytoplasmic  $\text{Ca}^{2+}$  signals in growing and Sen Doxo cells challenge with FCCP using Fluo-4AM. Bar graph: Quantification of peak Fluo-4AM fluorescence ( $N = 3$ , Mean  $\pm$  SEM. 20 cells were analyzed in each experiment).  $*p < 0.05$ , t test). **I** Confocal image of GEM-GECO1<sub>mito</sub> fluorescence from growing and Sen Doxo IMR90 cells captured at wavelengths 470–500 nm, at wavelengths

>520 nm and their overlay. The bar graph compares mean resting  $[\text{Ca}^{2+}]_{\text{mito}}$  (estimated as F470–500/F > 520) in growing and Sen Doxo IMR90 cells ( $N = 3$ , mean  $\pm$  SEM. 12 cells were analyzed,  $***p < 0.001$ , t test). **J** Representative traces of cytoplasmic  $\text{Ca}^{2+}$  signals in growing, Sen Doxo and Sen Eto cells challenge with histamine using Fluo-4AM. Bar graph: Quantification of peak Fluo-4AM fluorescence ( $N = 3$ , Mean  $\pm$  SEM. 50–80 cells were analyzed in each experiment).  $****p \leq 0.0001$  ANOVA test). **K** Representative Western blot of MERCS proteins in growing, Sen Doxo, and Sen Eto. Bar graphs are expressed as average fold change over basal levels (growing cells).  $N = 3$ –6, mean  $\pm$  S.E. (ANOVA test). **L** Representative images of Proximity Ligation Assay (PLA) of the 3 IP3R isoforms with VDAC1, and ER marker PDI with VDAC1 in growing, Sen Doxo and Sen Eto cells. Bar graphs: Quantitative analysis of number of dots per cells ( $N = 3$ , mean  $\pm$  SEM. 20–50 cells were analyzed in each experiment).  $****p \leq 0.0001$ , ANOVA test). **M** Representative traces of cytoplasmic  $\text{Ca}^{2+}$  signals using Fluo-4AM in growing, Sen Doxo and Sen Eto cells treated with 5  $\mu\text{M}$  dmXeB for 1 h and challenge with histamine. ( $N = 3$ , Mean  $\pm$  SEM. 10–15 cells were analyzed in each experiment). **N** LIVE/DEAD assay to evaluate cellular viability ( $N = 4$ ;  $****p \leq 0.0001$ ,  $***p \leq 0.005$ , ANOVA test). **O** Representative fluorescence images of p16-3MR mice liver treated with two rounds of Doxo (30 mg/k) followed by four rounds of either dmXeB (30 mg/k) or ganciclovir. Bar graph: Quantitative analysis of fluorescence intensity ( $N = 4$ , Means  $\pm$  SEM. Control:  $404.2 \pm 19.6$ , Doxo:  $444.6 \pm 11.6$ , Doxo + dmXeB:  $379.5 \pm 9.09$  and Doxo + GCV:  $407.5 \pm 32.0$  A.U. ANOVA test). **P** Upper panel. Representative images of SA- $\beta$ -gal staining of p16-3MR mice subcutaneous fat treated with two rounds of Doxo (30 mg/k) followed by four rounds of either DmXeB (30 mg/k) or ganciclovir. Bottom panel. Subcutaneous fat with an optical mask used for analysis. Bar graph: Quantitative analysis of relative intensity ( $N = 4$ , Means  $\pm$  SEM. Control:  $39.24 \pm 13.54$ , Doxo:  $177.5 \pm 12.98$ , Doxo + dmXeB:  $54.79 \pm 10.83$  and Doxo + GCV:  $62.74 \pm 23.22$  R.U. ANOVA test).

there are changes in heterotetramer stoichiometries as well as in receptor licensing.

We acknowledge that our study is limited to IMR-90 cells, and further investigations are warranted in other mesenchymal and epithelial cell types. Additionally, while our findings pertain to topoisomerase inhibitors, it remains unknown whether similar outcomes can be replicated with different classes of chemotherapeutic agents that induce senescence. A significant proportion of cancer survivors treated with chemotherapy experience accelerated aging and frailty, which have been associated with the presence of senescent cells<sup>15,16</sup>. Therefore, the discovery and development of senolytic treatments are fundamental to improving the quality of life for millions of individuals. While comprehensive experiments are necessary to validate the in vivo effects of dmXeB, including assessments of its long-term toxicity, the short-term treatment results, which show no signs of toxicity<sup>17</sup> are highly encouraging.

In conclusion, our findings reveal that TIS cells display an increase in MERCS alongside a reduction in mitochondrial  $\text{Ca}^{2+}$  flux, both of which are essential for sustaining the homeostatic state of these cells. The impaired  $\text{Ca}^{2+}$  transfer between the ER and mitochondria represents a critical vulnerability and an attractive target for senolysis in the context of TIS. Furthermore, dmXeB emerges as a compelling senolytic agent with potential therapeutic applications (Fig. 2).

## Methods

### Reagents

From Thermo Fisher Scientific (Waltham, Massachusetts, USA): Dulbecco's modified Eagle medium-high glucose (DMEM-HG) (12100-046), DMEM-HG no glutamine and calcium (21068028), trypsin (0.25%)–EDTA phenol red (25200072), antibiotic-antimycotic (100 $\times$ ) (15240062), trypan Blue solution 0.4% (15250061), Opti-MEM<sup>™</sup> GlutaMAX<sup>™</sup> supplemented (51985034), DMEM FluoroBrite<sup>™</sup> (A1896701), Fluo-4/AM (F-14201), Rhod2/AM (R-1245MP), Lipofectamine<sup>™</sup> 3000 (L3000015), Lipofectamine<sup>™</sup> RNAiMAX (13778150), TMRE (T669), Hoechst 33342 (H3570), Fluoromount-G mounting medium (00-4958-02), Pierce<sup>™</sup> Bradford plus protein assay (23236), SuperSignal<sup>™</sup> West Pico PLUS chemiluminescent substrate (34580), PageRuler<sup>™</sup> Plus prestained protein ladder (26619), Image-iT<sup>™</sup> fixative solution (FB002), X-Gal (B-1690). From Cytiva

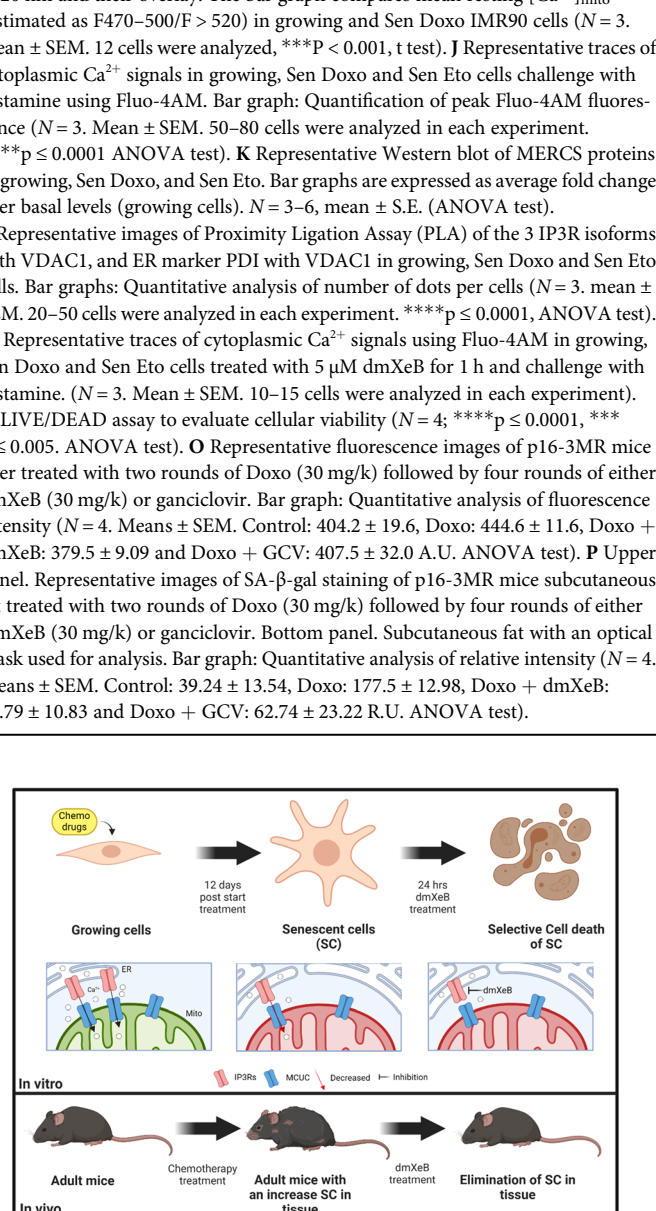


**Fig. 2 | Mechanistic overview of therapy-induced senescence (TIS) vulnerabilities and senolytic action of dmXeB.** Schematic representation illustrating the interplay between mitochondria and the endoplasmic reticulum (ER) in TIS cells. Therapy-induced senescence, triggered by chemotherapeutic agents such as Doxorubicin and Etoposide, leads to an increase in mitochondria-ER contact sites (MERCS) but a reduction in ER-to-mitochondria  $\text{Ca}^{2+}$  flux. This is associated with decreased expression of IP3R isoforms and disrupted IP3R1-VDAC interactions, impairing  $\text{Ca}^{2+}$  transfer while preserving MERCS integrity. dmXeB, an IP3R inhibitor, selectively targets TIS cells by further inhibiting ER-mitochondria  $\text{Ca}^{2+}$  flux, inducing apoptotic-like cell death via mechanisms partially dependent on necroptosis and caspase pathways. In vivo, dmXeB effectively reduces senescent cell burden in aged p16-3MR transgenic mice, as evidenced by decreased p16 fluorescence in liver tissue and reduced SA- $\beta$ -galactosidase staining in subcutaneous fat. This figure highlights a novel therapeutic strategy targeting  $\text{Ca}^{2+}$  signaling vulnerabilities in senescent cells.

(Chicago, Illinois, USA): Fetal bovine serum (HC.SV30160.03), Amersham Hybond P 0.45 PVDF blotting membrane (10600023). From Sigma-Aldrich (St. Louis, Missouri, USA): Histamine dihydrochloride (H7250-5G), PLA Duolink<sup>®</sup> (DUO92014-100RXN), carbonyl cyanide 4-(trifluoromethoxy) phenylhydrazone (FCCP) (C2920), protease Inhibitor Cocktail (P2714), PhosSTOP<sup>™</sup> (4906837001). From Tocris Bioscience (Bristol, United

Kingdom): From *Merck* (Darmstadt, Alemania): Acrylamide bis-acrylamide 29:1, 40% solution (1690-OP), triton® X-100 (112298), methanol (106009), 10× PBS (6505-OP), dimethyl sulfoxide (317275), hydrochloric acid fuming 37% (100317), sodium hydroxide (106498), TWEEN® 20 (655205), RIPA buffer (20–188). From *Santa Cruz Biotechnology* (Dallas, Texas, EE. UU.): BSA (sc-2323), Z-VAD-FMK (Z-VAD) (sc-3067). From *Winkler* (Santiago, RM, Chile): TRIS buffer (BM-0585), glycerol (BM-0800), 2-mercaptoethanol (BM-1200), SDS (BM-1750), bromophenol blue (AZ-0395), glycine (BM-0820), methanol (AL-0210), glutaraldehyde (WK-106), NaCl (SO-1455), KCl (PO-1260), Tween-20 (016520).

**Plasmids.** From *Addgene* (Watertown, MA, USA.): pCAG mito-GCaMP5G (105009), CMV-mito-GEM-GECO1 (32461), BFP-KDEL (49150).

**Antibodies.** From *Cell Signaling Technology* (Danvers, MA, USA): anti-IP<sub>3</sub>R1 (8568), anti-MCU (14997), anti-p21 Waf1/Cip1 (12D1) (2947), anti-MCU (D2Z3B), anti-MICU1 (D4P8Q). GRP75 (D13H4) (3593S), PDI (C81H6) (3501S). From *Abcam* (Cambridge, UK): anti-VDAC1 (AB10527), anti-VDAC1 (AB14734), anti-TOMM20 (AB56783), anti-cleaved caspase-3 (AB32042), p16: CDKN2A/P16INK4a (ab108349). From *Becton & Dickinson* (Franklin Lakes, NJ, USA.): anti IP<sub>3</sub>R3 (610313). From *Thermo Fisher Scientific* (Waltham, Massachusetts, USA): Anti-IP<sub>3</sub>R2 (PA1-904), anti β-tubulin (32–2600), anti-mouse secondary antibody Alexa Fluor™ 350 (A11045), anti-rabbit secondary antibody Alexa Fluor™ 488 (A11008), anti-mouse secondary antibody Alexa Fluor™ 488 (A11001), anti-rabbit secondary antibody Alexa Fluor™ 568 (A11011), anti-mouse secondary antibody Alexa Fluor™ 568 (A11004), anti-rabbit secondary antibody Alexa Fluor™ 647 (A21244), anti-mouse secondary antibody Alexa Fluor™ 647 (A21235), anti-rabbit secondary antibody HRP (31460), anti-mouse secondary antibody HRP (31430). From *Santa Cruz Biotechnology* (Dallas, Texas, EE. UU.): anti-β-actin (sc-47778), anti-HSP90 (13119sc). From *Millipore* (Burlington, Massachusetts, EE. UU.): Anti-phospho-Histone H2A.X (Ser139) (05-636).

### Cell culture and treatment

IMR90 (ATCC® CCL186™) cell line was maintained in Dulbecco's modified Eagle's medium, supplemented with 10% fetal bovine serum (FBS; *Biological Industries*), 100 U/ml penicillin, 100 mg/ml streptomycin and 0.25 µg/ml amphotericin B (antibiotic-antimycotic solution), at 37 °C, 10% CO<sub>2</sub> and 3% O<sub>2</sub>. To induce senescence experiments, cells were incubated with 250 nm Doxorubicin or 10 µM Etoposide for 48 h, and the culture medium was refreshed every 2 days. All cell counts were performed manually by using ImageJ and performed in at least three independent replicates. From each replicate, 100 cells were counted. All experiments, both control and cells at the start of doxorubicin treatments, were conducted using between 5000 and 10,000 cells per cm<sup>2</sup>.

### Detection of SA-β-Gal

SA-β-Gal activity was evaluated as previously described in ref. 18.

### Multiplex Luminex assay of cytokines

Serum-free media from 24 h were collected and centrifuged at 1000 × g for 10 minutes to eliminate cell debris. The conditioned media were stored at -80 °C until use. A Human Luminex Discovery Assay of IL1α, ILβ, IL6, CXCL1 and MMP3 available in the kit were performed using the Customization Tool. Serial dilution techniques were used to quantify the concentrations of cytokines, following the manufacturers' recommendations using Luminex MAGPIX Analyzer, and the results were expressed as pg/mL.

### Live imaging

For ER labeling, 1 µg of ER-BFP expression vector (mBFP fused to KDEL) was transfected in transfection medium and Lipofectamine 3000, according

to the manufacturer's instructions. For mitochondrial labeling, TMRE was used at a concentration of 10 nM, incubated for 20 min at RT (room temperature). Images were acquired using a TCS SP8 confocal microscope (Leica, Wetzlar, Germany) and were taken in different channels, then merged to evaluate the points of greatest proximity between ER-Mitochondria and their respective correlation coefficients known as Manders' coefficients. Finally, they were processed and analyzed using ImageJ software (NIH Image).

### Transmission electron microscopy

Cells were fixed using a specialized fixative mixture for electron microscopy (3% glutaraldehyde, 0.05% picric acid, and 50 mM sodium cacodylate buffer) for 10 minutes. Subsequently, the cells were mechanically detached from the plate and centrifuged at 3000 rpm for 5 minutes. The resulting pellet was incubated overnight in the electron microscopy fixative solution.

The samples were then washed multiple times with sodium cacodylate buffer and post-fixed with 1% osmium tetroxide in cacodylate buffer for 2 hours. Dehydration was carried out using a graded ethanol series, progressing from lower to higher concentrations, and concluded with an acetone bath. The samples were then infiltrated with acetone and Epon resin in increasing concentrations, ultimately embedding the samples in concentrated Epon resin.

Block processing, ultrathin sectioning, grid mounting, and imaging were conducted at the laboratory of Dr. José Manuel Villalba, from the Department of Cell Biology, Physiology, and Immunology at the University of Córdoba, Spain.

Images of mitochondria were taken at ×60,000 magnification. From these images, those showing interactions with the endoplasmic reticulum (ER) at distances between 10 and 50 nm were selected. In these selected images, the distance between the reticular membrane and the outer mitochondrial membrane was measured, as well as the percentage of mitochondrial surface covered by the ER. Image analysis was performed using ImageJ software (NIH Image).

### Plasmid transfection

**Plasmid transfection** was performed using Lipofectamine™ 3000 (Thermo Fisher Scientific) on cells plated in 6-well plate. Transfection mixture was prepared considering 2 µg/well of plasmid DNA, 5 µL P3000 and 10 µL Lipofectamine™ 3000 diluted in Opti-MEM. After 12 h the culture media were replaced with fresh medium and cells were incubated at 37 °C in a 5% CO<sub>2</sub> and 3% O<sub>2</sub> incubator. The experiments were performed 24–48 h post-transfection.

### Cell viability

Viability assays was determined using LIVE/DEAD Cell Imaging Kit (R37601) according to manufacturer's instructions. Images were obtained using confocal microscopy (TCS SP8 Spectral Confocal Microscope; Leica™) and subsequently processed and analyzed using ImageJ software (NIH).

### Measurement of cytoplasmic and mitochondrial Ca<sup>2+</sup> signals

Cells were grown on 18 mm Ø glass coverslips in 6-well plates and cytoplasmic and mitochondrial Ca<sup>2+</sup> signals were evaluated by *timelapse* in confocal microscopy, using Nikon C<sup>2+</sup> Confocal Microscope System (Nikon™), or Leica TCS SP8 Confocal Laser Scanning Microscope (Leica™) with control of temperature (37 °C), humidity and CO<sub>2</sub> (5%). Measurements were performed in calcium-free medium, using DMEM no calcium (Gibco™ #21068) supplemented with 100 µM EGTA.

**Cytoplasmic Ca<sup>2+</sup> signals.** IP<sub>3</sub>R activity was evaluated using the Ca<sup>2+</sup> sensitive cytoplasmic probe Fluo-4/AM (Max. ex/em: 494/506 nm). IMR90 cells growth in coverslips were loaded with 5 µM Fluo-4/AM (30 min) in complete medium and mounted in round chamber for microscopy imaging. The cells were washed twice with calcium-free medium and imaged in presence of the corresponding compounds. After a period of baseline recording, the cells were stimulated with a pulse of

0,3 mM histamine to induce IP<sub>3</sub>R-mediated Ca<sup>2+</sup> release. A total of 80 to 100 frames were recorded every 1.5 seconds approximately, at 488 nm excitation and using a  $\times 63$  objective. Images were analyzed and quantified using ImageJ (NIH).

**Mitochondrial Ca<sup>2+</sup> signals.** Mitochondrial Ca<sup>2+</sup> uptake from IP<sub>3</sub>R-mediated Ca<sup>2+</sup> release after histamine stimuli was determined initially using the mitochondria-targeted genetically encoded fluorescent Ca<sup>2+</sup> indicator mito-GCaMP5G t ( $K_d$  = 160 nM; Max. ex/em: 488/500 and 550 nm). For these experiments, cells were transfected with plasmid DNA (2  $\mu$ g/well on 6-well plates) using lipofectamine 3000. After 24 h pos-transfection, cells were trypsinized, seeded on 25 mm Ø glass coverslips and finally cultured for 24 h. Confocal image recording was performed as described above, at 488 nm excitation laser. In addition, we used Rhod-2/AM (Max. ex/em: 552/581 nm) to measure mitochondrial Ca<sup>2+</sup> signals, co-localized with the mitotracker green FM (Max. ex/em: 490/516 nm) labeling. For this approach, cells seeded on 25 mm Ø glass coverslips were loaded with 5  $\mu$ M Rhod-2/AM and 100 nM mitotracker green FM (30 min) in complete medium after completion of the experimental treatments. For the confocal timelapse, cells were mounted in the microscope chambers, washed twice with calcium-free medium, and finally recorded before and after the stimulation with 0,3 mM histamine, using a  $\times 63$  objective, at 488 nm and 561 nm excitation lasers for mitotracker green FM and Rhod-2/AM respectively. In addition, we used an FCCP stimuli to uncouple mitochondrial membrane potential, after a period of baseline recording. This resulted in the release of mitochondrial Ca<sup>2+</sup>, which was measured in the cytoplasm using the Fluo-4/AM probe. IMR90 cells were loaded with 5  $\mu$ M Fluo-4/AM for 30 minutes in complete medium, as previously described. A total of 140 frames were recorded every 1.5 seconds approximately. Images were analyzed and quantified using ImageJ (NIH).

Finally, basal mitochondrial Ca<sup>2+</sup> levels were measured as described in ref. 19.

### Protein extraction and quantification

Cells seeded in 6-well plates were cultured for 24 h and then subjected to corresponding experimental treatments. Once treatments were finished, cells were placed on ice, washed twice with ice-cold PBS, and finally scraped and lysed using CytoBuster™ protein extraction reagent supplemented with protease and phosphatase inhibitors. The obtained homogenates were sonicated, incubated 15 minutes on ice, centrifuged at 12,500  $\times$  rpm for 20 minutes at 4 °C, and the supernatant was collected. Protein quantification was performed using the Bradford method in 96-well plates, and OD<sub>595</sub> nm was determined using the Infinite 200 PRO plate reader (Tecan™).

### SDS-PAGE and western blotting

Protein extracts were mixed with sample buffer 5 $\times$  (250 mM Tris-HCl; 40% v/v glycerol; 8% v/v 2-mercaptoethanol; 10% w/v SDS; 0,5% w/v bromophenol blue, pH 6.8) and then boiled for 5 minutes at 100 °C. Once cooled, 30  $\mu$ g of protein extract from each sample was separated electrophoretically in either 5%, 10% or 15% SDS-polyacrylamide gels using a Mini-PROTEAN Tetra Cell (Bio-Rad™) with running buffer containing: 25 mM Tris; 192 mM glycine; 0,1% w/v SDS at pH 8.3, and subsequently transferred to PVDF membranes by Trans-Blot™ SD Semi-Dry Transfer Cell (Bio-Rad ®). Membranes were subsequently blocked 60 minutes with 5% w/v bovine serum albumin (BSA) prepared in Tris buffered saline-tween (TBS-T) containing: 20 mM Tris-HCl, 150 mM NaCl and 0.05% w/v Tween 20, at pH 7.5. Corresponding primary antibodies (dilution 1:1000 or 1:3000) were incubated overnight at 4 °C, then washed with TBS-T and subsequently incubated with HRP-conjugated secondary antibody (dilution 1:2000) for 1 h at room temperature with shaking. Protein signal was visualized using SuperSignal™ West Pico PLUS chemiluminescent substrate and documented with ChemiDoc™ Imaging System (Bio-Rad). Images were analyzed and quantified using ImageJ (NIH).

### PLA

For Immunofluorescence and PLA assays, 5000 cells per cm<sup>2</sup> were seeded on 12 mm Ø glass coverslips. Once the corresponding experimental treatments were completed, cells were fixed with 4% w/v paraformaldehyde (Image-iT™ fixative solution; Thermo Fisher Scientific), washed in PBS, then permeabilized in 0.1% v/v triton X-100 in PBS and blocked for 1 h in 10% w/v BSA in PBS at room temperature. After blocking, cells were incubated with the indicated antibodies; overnight at 4 °C followed by Duolink manufacturer's instructions (Duolink, Sigma-Aldrich). Once incubation was completed, cells were washed 3 times in PBS and Hoechst 33342 was applied during the last wash. The coverslips were mounted on slides using the mounting medium Fluoromount-G™. Images were obtained using confocal microscopy (TCS SP8 Spectral Confocal Microscope; Leica™) and subsequently processed and analyzed using ImageJ software (NIH).

### Mice and doxorubicin-induced in vivo senescence

This study was carried out following the strict recommendations in the Guide for the Care and Use of Laboratory Animals of the National Institutes of Health. The animal protocol was approved by the Committee on the Ethics of Animal Experiments of Universidad Mayor (number:05/2020). Mice were provided standard chow ad libitum and maintained under a 12:12-hour light/dark cycle. Systemic cellular senescence was introduced by treating mice with doxorubicin, as described. Briefly, a single dose of doxorubicin (10 mg/kg) was injected intraperitoneally and/or ABT-263 inhibitor was administered by gavage. Organs (lung, kidney, and liver) were collected.

Fluorescence images of organs were captured by In-Vivo FX PRO (Bruker) imaging system. To obtain a white-black image, organs were exposed to the white light for 0.175 seconds and to obtain a fluorescent image, they were exposed to 530 nm excitation wavelength for 10 seconds, capturing the obtained fluorescence using a filter of 600 nm. Auto-fluorescence was corrected for each organ, respectively to the non-treated control auto-fluorescence. Subsequently, a merge of both images, white-black and fluorescence, was created, and a representative image was constructed. Graphics of fluorescence quantification were created using the obtained mean intensity by each organ n = 4.

### Statistical analysis

Depending on the type of experiment, the results are shown as representative images or mean  $\pm$  SEM of at least 3 independent experiments. Statistical analyses were performed using Prism 8 software (GraphPad software). Significance of differences was assessed using unpaired t-tests. In the case of data that exhibited a normal distribution, the data were analyzed using a T-Test and one-way ANOVA with comparisons among the different experimental groups using Sidak correction. Additionally, comparisons were made with the control group using Dunnett's test correction. Differences with a *p* value  $< 0.05$  were considered statistically significant.

### Data availability

Data, materials, methods and supporting data is available from the authors upon request.

Received: 27 June 2024; Accepted: 17 January 2025;

Published online: 21 February 2025

### References

1. Di Micco, R., Krizhanovsky, V., Baker, D. & d'Adda di Fagagna, F. Cellular senescence in ageing: from mechanisms to therapeutic opportunities. *Nat. Rev. Mol. Cell Biol.* **22**, 75–95 (2021).
2. Hernandez-Segura, A., Nehme, J. & Demaria, M. Hallmarks of cellular senescence. *Trends Cell Biol.* **28**, 436–453 (2018).
3. El, H., Martini, Ene, Ao, J., Passos, F. & Passos, J. F. Cellular senescence: all roads lead to mitochondria. *FEBS J.* **290**, 1186–1202 (2023).

4. Csordás, G., Weaver, D. & Hajnóczky, G. Endoplasmic reticulum–mitochondrial contactology: structure and signaling functions. *Trends Cell Biol.* **28**, 523–540 (2018).
5. Ziegler, D. V. et al. Calcium channel ITPR2 and mitochondria-ER contacts promote cellular senescence and aging. *Nat. Commun.* **12**, 720 (2021).
6. Farfariello, V. et al. TRPC3 shapes the ER-mitochondria Ca<sup>2+</sup> transfer characterizing tumour-promoting senescence. *Nat. Commun.* **13**, 956 (2022).
7. Madreiter-Sokolowski, C. T. et al. Enhanced inter-compartmental Ca<sup>2+</sup> flux modulates mitochondrial metabolism and apoptotic threshold during aging. *Redox Biol.* **20**, 458–466 (2019).
8. Gao, Y. et al. Calcium transferring from ER to mitochondria via miR-129/ITPR2 axis controls cellular senescence in vitro and in vivo. *Mech. Ageing Dev.* **218**, 111902 (2024).
9. Podunavac, M. et al. Scalable total synthesis, IP3R inhibitory activity of desmethylxestospongin B, and effect on mitochondrial function and cancer cell survival. *Angew. Chem. Int. Ed. Engl.* **60**, 11278–11282 (2021).
10. Chang, J. et al. Clearance of senescent cells by ABT263 rejuvenates aged hematopoietic stem cells in mice. *Nat. Med.* **22**, 78–83 (2016).
11. Demaria, M. et al. An essential role for senescent cells in optimal wound healing through secretion of PDGF-AA. *Dev. Cell* **31**, 722–733 (2014).
12. Ast, T. & Mootha, V. K. Oxygen and mammalian cell culture: are we repeating the experiment of Dr. Ox? *Nat. Metab.* **1**, 858–860 (2019).
13. Parrinello, S. et al. Oxygen sensitivity severely limits the replicative lifespan of murine fibroblasts. *Nat. Cell Biol.* **5**, 741–747 (2003).
14. van Vliet, T. et al. Physiological hypoxia restrains the senescence-associated secretory phenotype via AMPK-mediated mTOR suppression. *Mol. Cell* **81**, 2041–2052.e6 (2021).
15. Ness, K. K. & Wogksch, M. D. Frailty and aging in cancer survivors. *Transl. Res.* **221**, 65–82 (2020).
16. Wang S., El Jundi N., Thyagarajan B., Prizment A., Blaes A. H. Accelerated aging in cancer survivors: cellular senescence, frailty, and possible opportunities for interventions. *Int. J Mol. Sci.* **25**, 3319 (2024).
17. Bustos, G. et al. The IP3R inhibitor desmethylxestospongin B reduces tumor cell migration, invasion and metastasis by impairing lysosome acidification and  $\beta$ 1-integrin recycling. *Biochim. Biophys. Acta* **1871**, 167557 (2025).
18. Debacq-Chainiaux, F., Erusalimsky, J. D., Campisi, J., Toussaint, O. Protocols to detect senescence-associated beta-galactosidase (SA- $\beta$ gal) activity, a biomarker of senescent cells in culture and in vivo. *Nat. Protoc.* **4**, 1798–806 (2009).
19. Farfariello, V. et al. TRPC3 shapes the ER-mitochondria Ca<sup>2+</sup> transfer characterizing tumour-promoting senescence. *Nat. Commun.* **13**, 956 (2022).

## Acknowledgements

We thank Judith Campisi and Pierre-Yves Desprez from the Buck Institute for Research on Aging for their mentorship and for guiding us in establishing TIS models. We thank the Unidad de Microscopía Universidad Mayor, UM<sup>21</sup>

for their support during imaging. This work was supported by ANID/FONDECYT #1200255 (CC), #1240807 (CC) and ANID/FONDAP #15150012 (CC, CGB). ANID/FONDECYT postdoctoral fellowships #3220593 (UAC), #3230273 (GB), #3220604 (ESP) and # 3230476 (SLS). ANID scholarship #21212019 (PMC), Universidad Mayor Scholarship (C.C-C). ANID/FONDAP #15130011 (MJK). FPI predoctoral contract funded by MINECO (reference BES-2016-078229) (SRL). NIH RO1 077379 (AZ).

## Author contributions

U.A-C and C.C., designed and wrote the manuscript. U.A-C and S.A.N. performed Ca<sup>2+</sup> experiments. U.A-C, A.P-H, C.Q and G.B. performed confocal microscopy experiments and Western blotting. E.S-P, P.M-C, and C.C-C, performed cytometry assay. O.D-R performed plasmid extraction. U.A-C, J.A.L-D, S.R-L, and J.M.V. performed TEM experiments. H.H, G.Q, C.G-S, S.L., E.S-H, and M.J.K. conducted mice experiments. H.H. performed cytokine measurements. A.L., C.G-B, J.M., and A.Z. contributed to the interpretation of the results and provided feedback. All authors read and approved the final manuscript.

## Competing interests

The authors declare the following financial interests/personal relationships which may be considered as potential competing interests: Armen Zakarian and J. César Cárdenas hold a patent on the synthesis of dmXeB.

## Additional information

**Correspondence** and requests for materials should be addressed to Ulises Ahumada-Castro or J. César Cárdenas.

**Reprints and permissions information** is available at <http://www.nature.com/reprints>

**Publisher's note** Springer Nature remains neutral with regard to jurisdictional claims in published maps and institutional affiliations.

**Open Access** This article is licensed under a Creative Commons Attribution-NonCommercial-NoDerivatives 4.0 International License, which permits any non-commercial use, sharing, distribution and reproduction in any medium or format, as long as you give appropriate credit to the original author(s) and the source, provide a link to the Creative Commons licence, and indicate if you modified the licensed material. You do not have permission under this licence to share adapted material derived from this article or parts of it. The images or other third party material in this article are included in the article's Creative Commons licence, unless indicated otherwise in a credit line to the material. If material is not included in the article's Creative Commons licence and your intended use is not permitted by statutory regulation or exceeds the permitted use, you will need to obtain permission directly from the copyright holder. To view a copy of this licence, visit <http://creativecommons.org/licenses/by-nc-nd/4.0/>.

© The Author(s) 2025